Controlled Loads on an Axisymmetric Platform at High Incidence using Forebody Aerodynamic Bleed

Edward Lee [1], Bojan Vukasinovic[2], and Ari Glezer[3]
Woodruff School of Mechanical Engineering,
Georgia Institute of Technology, Atlanta, GA 30332-0405

Abstract

The aerodynamic loads exerted on a cylindrical platform model at high angles of attack ($35^o < \alpha < 55^o$) are manipulated in wind tunnel experiments using distributed bleed actuation on its forebody. The asymmetry of the counter rotating forebody vortex pair that forms over the forebody and leads to asymmetric side forces and yawing moment at high incidences is exploited for control of these loads using azimuthally segmented bleed effected over the forebody. In the present investigations, bleed actuation is effected either for suppression or enhancement of these asymmetric loads. It is demonstrated that by direct control of the forebody vortices, segmented bleed can effectively attenuate the randomly evolving loads and/or effect prescribed side load. It is shown that over the present range of angles of incidence segmented bleed configurations can lead to significant changes in controlled side force of up to $\Delta C_S = \pm 3.5$ with minimal changes in lift and drag (for reference $C_L \approx 4.5$).

I. Background

The flow about axisymmetric cylindrical bodies at high angles of incidence have been widely investigated with the objective of improving the aerodynamic performance of various flight platforms including missiles and rockets and fighter aircraft. The flow and aerodynamic loads over such cylindrical bodies are dominated by a hierarchy of vortical structures that form in their wake and whose complexity and intricacy intensify with increasing incidence. The evolution of these vortices commences with the rollup of counter-rotating forebody vortex pair and progresses by streamwise-successive convective interactions with the shear layers that bound the near wake on the leeward side of the main cylinder.

The prior work points to the critical role of the symmetry in the evolution of the forebody vortices with changing angle of attack. As noted by Ericsson and Reding (1986) and Zilliac et al. (1991), the forebody vortices, which evolve symmetrically at low angles of attack, become asymmetric once the body pitch angle increases beyond a certain critical angle (arguably dependent on the forebody tip angle) and one of the forebody vortices detaches off the body prematurely. As discussed by Allen and Perkins (1951), the asymmetric vortex flow developed at such a high inclination effects a net non-zero side force and yawing moment that are undesirable from the platform control perspective. Subsequent investigations focused on identifying the sources of this

[1] Graduate Research Assistant, AIAA Member.
[2] Research Engineer, AIAA Member.
[3] Professor, AIAA Fellow.

aerodynamic behavior. Keener and Chapman (1974) demonstrated that the onset pitch angle leading to asymmetry of the forebody vortices is dependent on the forebody geometry, while Yanta and Wardlaw (1977, 1981) attributed asymmetry in the vortex pair evolution at high inclinations to minor variations of the surface of a nominally axisymmetric forebody. In a numerical investigation, DeSpirito (2017) included spin stabilization in studies of the net side forces at both below and above the onset of the asymmetry. Nnumerous studies (e.g., Thomson and Morrison 1971, Keener and Chapman 1974, Lamont 1982, and more recently Mahadevan et al., 2018) demonstrated that the sensitivity of the vortices is related to the surface imperfections that typically lead to variations in the net induced side forces with changes in azimuthal forebody orientation.

The prior studies that indicated the sensitivity of the evolution the forebody vortex pair to small surface perturbations also pointed out to a path of exploiting this sensitivity for controlling the aerodynamic loads with minimal control input. Therefore, various forebody flow control techniques have been developed to directly manipulate the evolution of the forebody vortices for alleviation of undesired side forces and yawing moments of the flight platforms caused by asymmetric vortex coupling to the wake. Addition of passive features on the forebody have been examined by Xueying et al. (2002) with spherical and rectangular shaped perturbation near the forebody tip to influence bi-stable realization of forebody vortices, following Ericsson and Reding (1980) who evaluated the effect of trip wires on the forebody to relieve the vortex-induced side loads. Besides passive means, studies of active flow control using jet actuation near the forebody have also been conducted. Leu et al. (2005) used an array of inflatable micro-balloon actuators installed on the surface of a conical forebody to induce the formation of asymmetric vortices and thereby the side forces of a desired direction. Kumar et al. (2008) introduced a mechanism with a control jet issuing axially from the forebody tip into the oncoming flow. They demonstrated that side force alleviation was proportional to ratio of the velocities of the jet and the free stream and attributed it to the "fluid dynamic blunting" by the jet. An indirect control of the forebody vortices was proposed by Lee et al. (2021a) who used a synthetic jet to control the wake at the forebody juncture and thereby alter the resulting net side forces. In a follow-on investigation, Lee et al. (2021b) extended this indirect forebody vortex control to suppress instabilities of the axisymmetric model at a narrow subrange of the high angles of attack.

Another approach to delay the side force, relevant to the present study, was tested on a forebody model by progressively perforating the increasing axial extent of the forebody and utilizing the aerodynamic bleed driven by pressure differences to enforce flow symmetry (Bauer and Hemsch, 1994). They showed that the increase in incidence of the onset of a nonzero side force was proportional to the axial extent of the bleed. In a similar application, Fears (1995) reported comparable results when replacing the solid forebody of a fighter aircraft model with a porous forebody as an alternative to control by strakes for generating yawing moment.

The present investigation is motivated by the findings of Bauer and Hemsch (1994) and focuses on exploiting segmented porosity over the forebody of a cylindrical platform for suppression of asymmetric baseline side forces that arise from flow sensitivity to minor imperfections of the body surface. Furthermore, configurations of segmented bleed actuation are also used for prescribing desired side forces and yawing moment for bi-directional aerodynamic control.

II. Experimental Setup and Procedures

The experimental investigation utilizes a slender axisymmetric model of a cylindrical body (diameter D = 50 mm, length $L = 9D$) with a tangent $2D$ long ogive forebody that can be rotated

azimuthally. This forebody was selected based prior studies (Lee et al., 2021a) which indicated that the forebody vortices on ogive forebodies induce higher side forces compared to other (e.g., conical) forebodies (e.g., Chapman et al, 1976). The present investigations focus on control of the forebody vortices that form autonomously over a range of angles of incidence ($35° < \alpha < 55°$) at cross stream speeds of up to $U_\infty = 30$ m/s ($Re_D = 9.9 \cdot 10^4$).

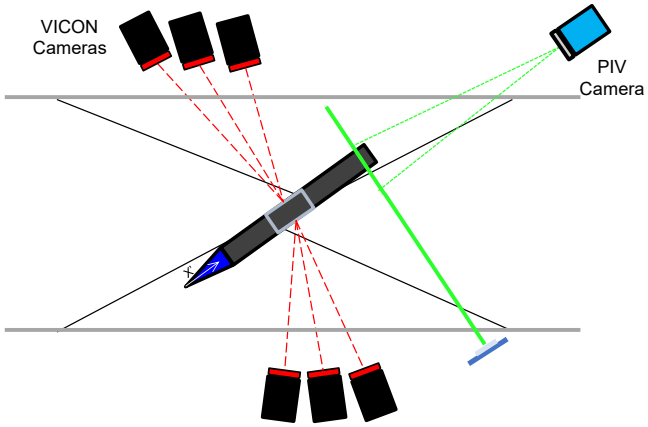

Figure 1. *A top view of the wire-supported model illustrating the PIV setup for measurements of the body-normal flow and the cameras that are used for tracking the model's position.*

The axisymmetric model is wire-supported in an open-return wind tunnel (test section measuring 91 cm on the side) by a dynamic 6-DOF eight-wire traversing mechanism (Figure 1) described in detail by Lambert et al. (2016). Each support wire has an in-line load cell and is controlled by an independent servo motor. The forces and moments on the model are calculated from the measured wire tensions projected onto the model (the resultant aerodynamic loads on the model are calculated relative to the loads in the absence of cross flow, and accounting for wire drag). The attitude of the model is commanded by a *MATLAB Simulink* controller, which feedback utilizes inputs from *VICON* motion-capture camera system at an update rate of 500 Hz. Besides providing the feedback signal, the six-camera motion capture system resolves the spatial and temporal position of the model at any instant in time. In an alternate configuration, the feedback loop can be disconnected with the model 'locked' in the desired attitude to simulate free-flight condition. Either configuration is utilized, depending on the body maneuvering. The information regarding the model position/orientation is used to extract the wire orientation and accurately decompose the forces measured on each load cell into x, y, and z components in real time. In addition to the measurement of the aerodynamic loads, a planar PIV system is used to characterize the model's forebody vortices and wake dynamics using a CCD camera aligned with the azimuthal axis (x' in Figure 1) of the model and placed downstream of the aft end of the model, imaging 532nm Nd:YAG laser sheet such that the measurement plane is normal to the model's axis at several axial stations, as illustrated schematically in Figure 1. Such PIV orientation enables investigations of the near-surface flow and the advection of streamwise vorticity concentrations into the near wake. Taligoski et al. (2015) demonstrated that, with a similar optical setup, it was possible to capture cross flow velocity field near the surface of the model. In the present investigations, 1,000 instantaneous PIV images are acquired at 1 kHz at $x'/D = 1.6$, 2.2, 4.0, 6.0, and 8.4 from the tip of the model's forebody at inclination of $\alpha = 50°$. Schematics in Figure 1 also illustrates orientations of the six motion-capture cameras that are distributed evenly on both sides of the test section.

The axisymmetric body is comprised of three major modules: the ogive forebody, the central cylindrical body, and the aft control module, which is kept inactive in the current investigation. The prior work (Lee et al., 2021a and 2021b) focused on direct control of the separating flow on

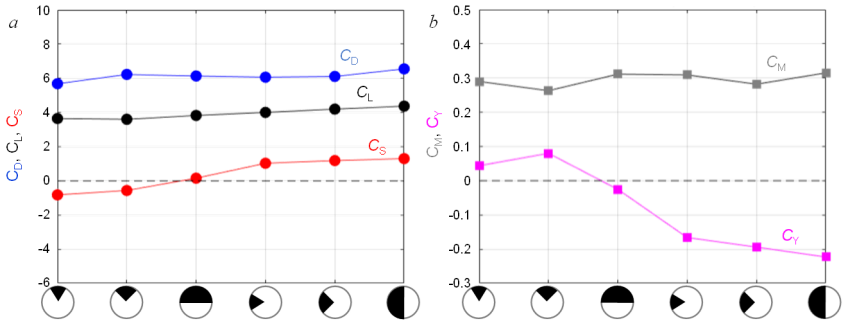

Figure 2. *The net aerodynamic force (a) and moment (b) coefficients for three azimuthal bleed extents: 45°, 90°, and 180°, represented by the shaded segments along the x-axis.*

the leeward side of the body, which, in turn, altered the dominant wake vortical composition through its inherent coupling. During the present investigation, the aerodynamic loads on the model are controlled by manipulation of the symmetry of the forebody vortices and, consequently, their interactions with the cylinder's wake using the aerodynamic bleed over the forebody. Therefore, while the earlier approach affected the dominant streamwise vortices, and consequently the aerodynamic loads, *indirectly* by focusing on their coupling to the wake along the cylindrical body, the present investigations focus on the *direct* control of the forebody vortices over their formation domain along the forebody. For that purpose, instead of the forebody with integrated fluidic actuation, a forebody with azimuthally distributed bleed ports is designed and manufactured, following the forebody bleed study of Bauer and Hemsch (1994). Initially, three different azimuthal extents of the bleed surface over the forebody are tested, spanning 45°, 90°, and 180° azimuth of the forebody, as illustrated in Figure 2 schematics. Each of these three configurations is tested in two orientations relative to the flow, by promoting the flow symmetry in the top-central orientation of each segment, and by promoting the flow asymmetry by orienting each segment to be centered on one side of the body. The resulting effects of these bleed configurations on aerodynamic loads are summarized in Figure 2. These preliminary results indicate that base flow suppression of asymmetry, expressed through the lowering of the resulting side force, increases with the azimuthal opening on the top of the forebody. In contrast with this, a minimal effect on the asymmetry is measured, as all the three configurations exerted nearly the same magnitude of the side force. Based on these preliminary findings, in spite of slightly better results achieved by half-the-circumference bleed application, it is decided to conduct a full investigation by utilizing a 90° bleed opening due to the limited number of orientations that the 180° bleed section would allow.

The bleed forebody model is shown in Figure 3, consisting of the outer and inner shell. Each azimuthal half of the outer shell is populated by the ten bleed rows, having the equal angular distribution, while each row consists of seven streamwise narrow bleed slots, as seen in Figure 3a-b. Different bleed configurations are formed by closing inactive ports, where the closed ports can be seen in light color in Figures 3a and b. Given the primary targeting of the two forebody vortices with an objective of both symmetric and asymmetric alterations of that vortex pair, a total of eight different bleed configurations are tested, as schematically represented in the bottom row of Figure 3. Dark azimuthal sections represent the active bleed segments, where most configurations represent different azimuthal orientations of the 90° bleed segment, except for a configuration having fully open bleed ports across the whole forebody surface. Therefore, the tested configurations, from left to right, included the fully closed (i.e., the base flow) and fully open configurations, top right, top and bottom left 90° segments, and the 90° segments centered at the left, top, and bottom.

III. Evolution of the Forebody Vortex Pair in the Base Flow

The present work particularly focuses on the forebody vortex pair evolution over the body, while the prior work (Lee et al., 2021a and 2021b) placed emphasis on the wake interactions of these vortices, both in the presence and absence of flow control. To illustrate the base flow over the model with all the bleed ports closed, the color raster plots of the streamwise vorticity relative to the body coordinate system (x') at five cross stream planes along the model are shown in Figure 4 for the pitch angle α = 50°. The initial formation of the forebody vortex pair at $x'/D = 1.6$ is reasonably symmetric and vortices have nearly identical magnitudes of vorticity (and its integral measure of circulation). The symmetry appears to be still preserved at $x'/D = 2.2$, where only the entrainment-driven growth of the vortices is measured. Some disruption in symmetry is noted at $x'/D = 4$, where both vortices begin to deflect away from the surface. By $x'/D = 6$, the two forebody vortices appear to have been grown away from the surface while still remaining attached to it, while the CW and CCW vortex sheets on both sides of the body's surface begin to roll up underneath the primary vortex pair. The asymmetry in the shedding of the forebody vortices downstream from x'/D = 6, as is evidenced by their trajectories, is manifested by an induced net right side force (along $y' < 0$) as a result of the earlier displacement of the CW vortex. The topology of the streamwise vorticity at $x'/D = 8.4$ indicates that the asymmetry propagates downstream, as the CW is seen displaced further into the wake than its corresponding CCW pair. Furthermore, formation of the secondary vortex pair about the cylindrical body continues underneath the displaced primary vortex pair, and their asymmetry further contributes to the net side force.

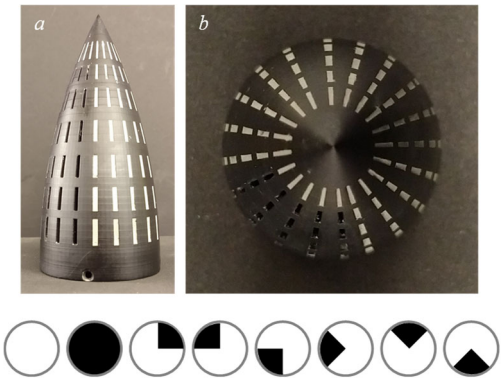

Figure 3. *Side (a) and top (b) views of the porous forebody model. Closed ports are off-white in color. Schematics in the bottom row illustrates eight bleed configurations, from left to right: fully closed (baseline), fully open, and the 90° open segments centered at the top right and left, bottom and center left, and at the top and bottom.*

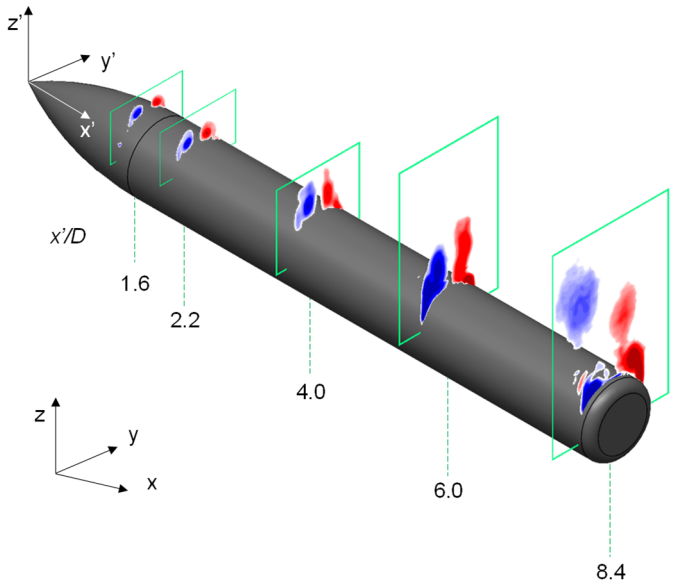

Figure 4. *Five PIV measurement planes showing color raster plots of concentrations of streamwise vorticity in the base flow over the cylinder.*

IV. Bleed-induced Vortex Asymmetry and Loads

As the first PIV measurement plane ($x'/D = 1.6$) is set right at the axial termination of the bleed, the corresponding flow fields are utilized for an initial assessment of the flow control effects for the fixed pitch angle α = 50°. Hence, all eight flow fields, corresponding to the eight bleed configurations depicted schematically in Figure 3, are shown in Figure 5 in terms of the mean

velocity field in the *y*'-*z*' plane (cf. Figure 4). The base flow (Figure 5a), in the absence of bleed, was already discussed with regard to Figure 4. The overall flow symmetry is emphasized by the symmetric vortices of nearly matched circulation magnitudes. This base flow is first contrasted with the case when the aerodynamic bleed is fully opened across all of the bleed ports (Figure 5b). As it could be expected, the net bleed is driven from the pressure side of the surface along the bottom to the upper surface, having a rather dramatic effect on the vortex pair evolution. Consequently, the vortex cores are displaced away from the surface and weakened. It is interesting that they still preserve the symmetry and remain "attached" to the body through the folding vortex sheet off the lower section of the forebody. The localized bleed segments that target only one of the forebody vortices induce asymmetric vortical composition already in the first measurement plane. For instance, symmetrically switched bleed configurations at the top right (Figure 5c) and left (Figure 5d) side promote displacement of the vortex on that side, already inducing the vortex/side force imbalance over the forebody. Although not as pronounced as when the bleed segment is directly underneath the evolving vortex on the top left side, even in the case when the bleed segment is along the pressure side (bottom left, Figure 5e), the aerodynamic bleed induces imbalance in the vortex pair growth, by promoting the same-side vortex. Knowing the outcomes of the aerodynamic bleed across the top and bottom left segments, it is not surprising that by orienting the bleed segment such that half is in the upper and the other half in the lower hemisphere on the left (Figure 5f), the primary effect on the growth of the same-side vortex is approximately between the effects of the individual top and bottom segments – the bleed enhances the growth (and asymmetry) of that side vortex, but not as significantly as in the case of the top-segment flow manipulation. In a summary of the three same-side azimuthal orientations of the 90° bleed segment, it appears that the most effective approach in inducing the vortex pair asymmetry is the bleed manipulation directly underneath the evolution of the targeted vortex. Lastly, two additional bleed configurations targeting symmetrically both the left and right forebody vortices are done by centering the 90° bleed segment directly and the top (Figure 5g) and bottom (Figure 5h). Not surprisingly, symmetric application of bleed preserves the overall flow symmetry in both cases. It is interesting that in either case there is actually a very little change even in the vortex structure, where at most the vortex sheet along the surface becomes somewhat enhanced in the case of

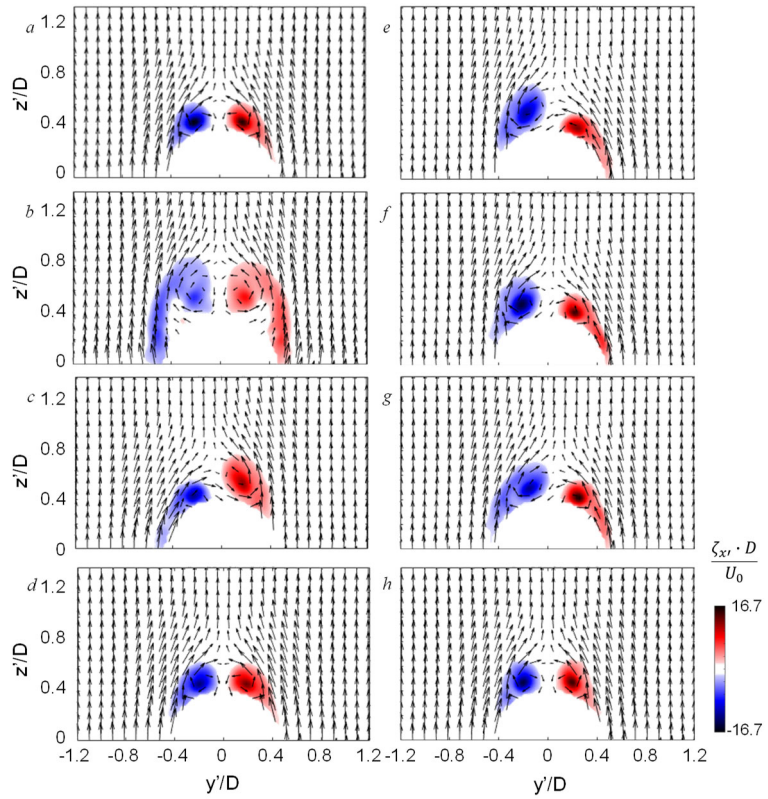

Figure 5. *Raster plots of the mean streamwise vorticity $\zeta_{x'}$ and in-plane velocity vectors at x'/D = 1.6 for the base flow (a) and for the azimuthal bleed configurations: fully open (b) and the 90° open segments centered at the top right (c) and left (d), bottom (e) and center (f) left, and at the top (g) and bottom (h).*

the top centering, while there is no discernable difference relative to the base flow when the bleed segment is centered at the bottom, symmetrically along the pressure surface.

The resulting global effect of these different bleed configurations is assessed through a cumulative, net change of the aerodynamic forces and moments, which are all shown in Figure 6 with respect to the fixed coordinate system (x,y,z, Figure 4), where x-axis is aligned with the flow direction. As expected, the bleed-induced alteration of the vortex symmetry, which couples to the wake asymmetry, is reflected in the strongest effect on the side force coefficient C_S (Figure 6a). Cumulative asymmetry in the base flow results in the net side force coefficient of nearly $C_S = 1$, along with the net baseline lift and drag forces. It should be noted that the normal force relative to the model orientation ($F_{z'}$) decomposes into the lift (F_z) and drag (F_x) forces shown in terms of the coefficients C_L and C_D in Figure 6a. As the bleed control is applied over the full circumference of the forebody, there is a clear drop in the net side force, accompanied by the increase in both the drag and lift coefficients C_D and C_L, which implies that the lift force normal to the body $F_{z'}$ increases as

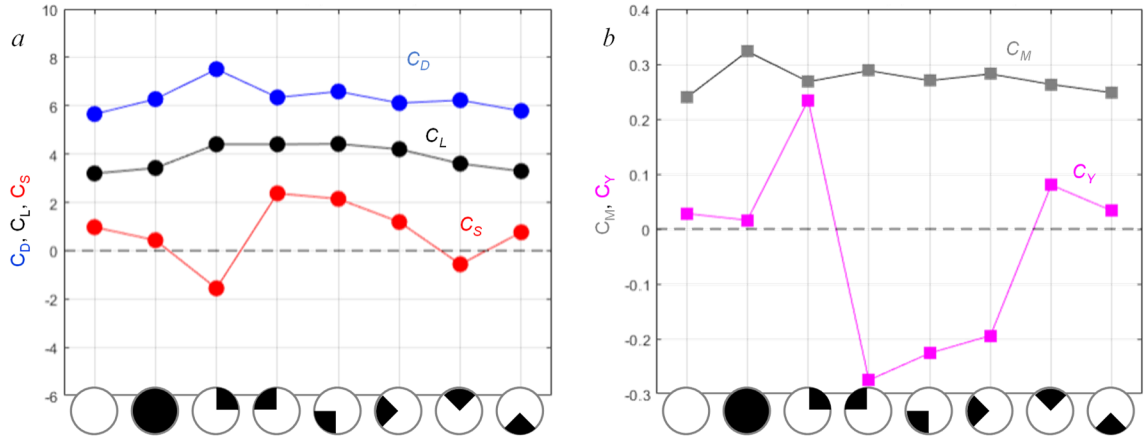

Figure 6. *The net aerodynamic forces (a) and moments (b) for the eight bleed configurations, schematically shown along the x-axis labels: fully closed (baseline), fully open, and the 90° open segments centered at the top right and left, bottom and center left, and at the top and bottom.*

well. As suggested by the altered flow field seen in Figure 5c, premature displacement of the CCW vortex by the bleed from the top right segment would contribute to the net negative side force, as seen in Figure 6a. Furthermore, there is an additional increase in both C_D and C_L, which also implies additional increase in the body-normal $F_{z'}$ force. In principle, a switch to the top left bleed segment is expected to generate the same and opposite effect from the top right segment. Indeed, there is a sharp switch in the side force to the net positive side, but some imbalance in magnitudes is attributed to the non-zero base flow, which is already 'biased' towards the net positive side force. It is interesting that the bottom-left bleed case is closer to an inverted top-right case in terms of all the three resulting aerodynamic forces. When the left-side bleed segment is azimuthally centered, the net side force remains positive but with a further reduction in magnitude, while the drag and lift forces remain practically unchanged. Finally, while the top-centered bleed segment reverses the net side force sign back to negative, the bottom-centered segment bleed does not effect much difference relative to the base flow. When assessing the bleed control effect on the moments (Figure 6b), it can be expected that the major changes seen in the side force F_y/C_S would translate in the corresponding dominant changes in the yaw moment C_Y. Indeed, Figure 6b indicates that there is negligible change in pitch C_M, while the most pronounced change is in the yaw moment. All the left-centered bleed

control tilts the yaw moment to the net negative, while the opposite sense and a similar to the magnitude in pitch is created by the top-right centered bleed control.

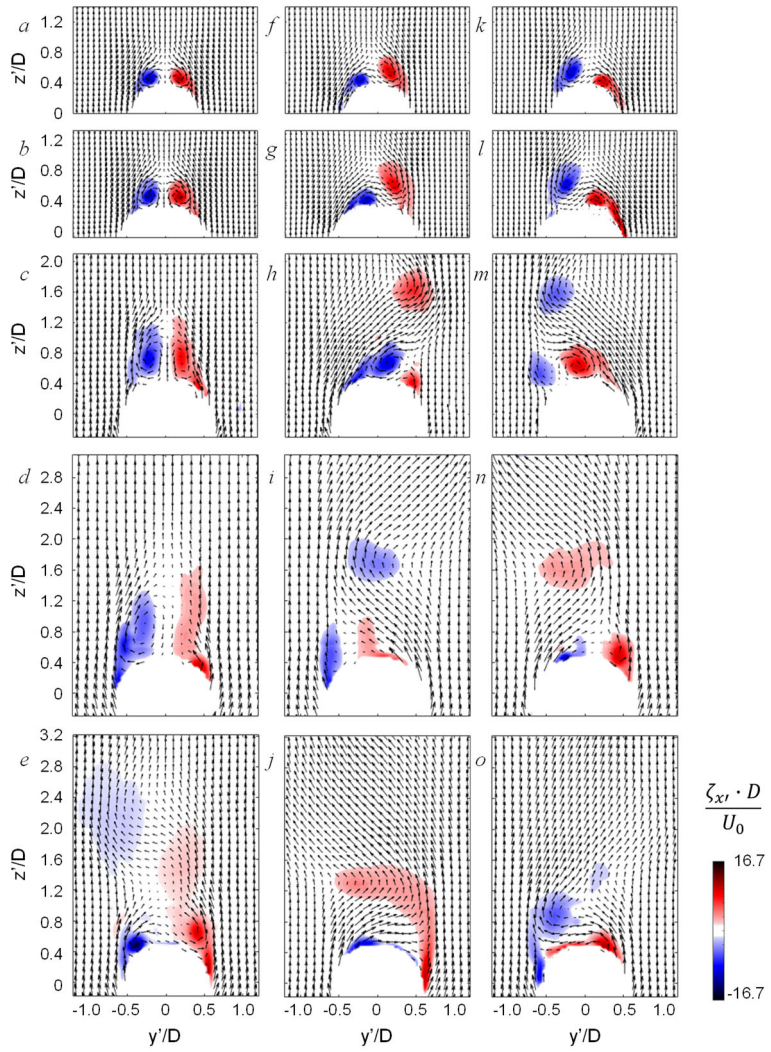

Figure 7. *Raster plots of the mean streamwise vorticity $\zeta_{x'}$ and in-plane velocity vectors at x'/D = 1.4 (a,f,l), 2.2 (b,g,m), 4 (c,h,n), 6 (d,j,o), and 8.4 (e,k,p) for the base flow (a–e) and for the 90°-open azimuthal bleed configurations across the top quarter right (f–k) and left (l–p) segments.*

Evolution of the flow fields for the two presumably most interesting control cases that provide the opposing net side forces and pitching moments is examined in closer detail in Figure 7, where the flow fields in all the five measurement planes (cf. Figure 4) are shown for both the segmented bleed control over the top quarter of the forebody on the right side and on the left side. In addition, the base flow field evolution, having the solid forebody, is included for reference. Besides illustrating how the surface vorticity rolls into two forebody vortices in the base flow, Figure 7a, along with the cross section at $x'/D = 2.2$ (Figure 7b) indicates a nearly perfect symmetry in the initial formation of both vortices. By $x'/D = 4$ (Figure 7c), vortices mainly grow in size and become displaced away from the surface, also indicating a possible onset of asymmetry. By the next measurement plane (Figure 7d), the vortices become notably elongated and lose some coherence – a possible indication of the increased unsteadiness. Finally, it becomes clear at the last measurement plane (Figure 7e) that the CW vortex separated off the body first, while the CCW vortex lags in the detachment. Another notable feature is that as soon as the primary vortex cores become sufficiently displaced off the surface, the continuing supply of the surface vorticity along the cylindrical body from below rolls into a secondary vortex pair, as clearly seen in Figure 7e. As suggested by the difference in the net side force magnitudes (of opposing signs) in Figure 6, it is expected that the flow field evolution for the top-right (Figures 7 f–j) and top-left (Figures 7 k–o) segmented bleed control would not be perfectly antisymmetric. Still, the dominant features are clearly antisymmetric. Right at the axial termination of the bleed control (Figures 7f and k), the vortex on the side of the activated bleed grows disproportionally and by $x'/D = 2.2$ (Figures 7g and l), it already begins to separate off the surface, while its counterpart's growth appears even inhibited relative to the base flow (cf. Figure 7b). The flow fields remain nearly antisymmetric even at the

next measurement plane (Figures 7h and m), where the already detached vortices still remain within the measured field of view. It is interesting to note that both counterparts of the detached vortices shift azimuthally along the top surface across the vertical plane of symmetry and affect the initial rollup of the secondary vortices underneath the detached primary ones. By the next measurement plane at $x'/D = 6$ (Figures 7i and n), the second primary vortex also becomes detached in either case, while their counterparts that were seen detached in Figures 7h and m are already outside of the measurement field of view. Some discrepancy in the overall anti-symmetry of the flow is seen in the pair of secondary vortex pairs that form along the body surface. However, the main feature of the azimuthal tilt of the remaining surface-bound vortices is seen in either case. As it was observed for the primary vortex detachment, the surface-bound vortex pair tilts azimuthally to the side of preceding vortex detachment. By the last measurement plane (Figures 7j and o), there is another strong switch in the vertical directionality of the wake above the body, having a stark contrast to only a weak disruption in the wake symmetry observed in the corresponding base flow (Figure 7e).

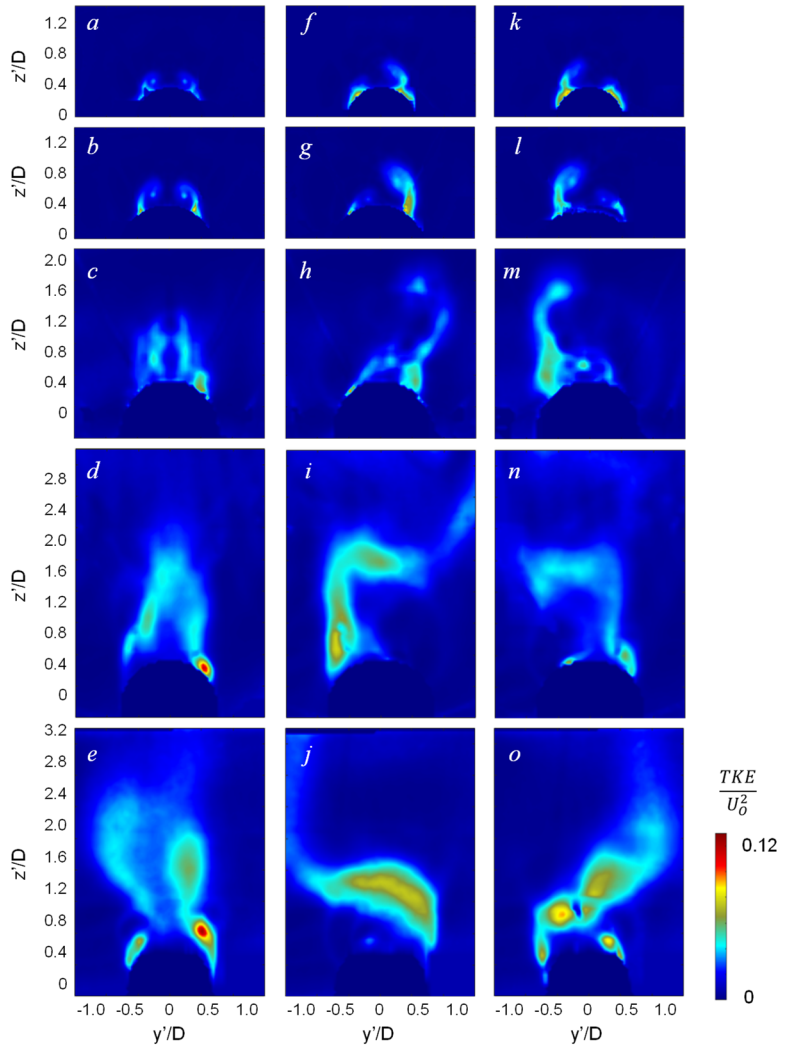

Figure 8. *Raster plots of the in-plane turbulent kinetic energy at x'/D = 1.4 (a,f,l), 2.2 (b,g,m), 4 (c,h,n), 6 (d,j,o), and 8.4 (e,k,p) for the base flow (a–e) and for the 90°-open azimuthal bleed configurations across the top quarter right (f–k) and left (l–p) segments.*

Aside from the vortical composition of the flow that was elucidated from Figure 7, there is additional interest in assessing the level of the flow unsteadiness, with and without the flow control. For that purpose, the in-plane contribution to the turbulent kinetic energy TKE = $\overline{v'^2} + \overline{w'^2}$ is shown in Figure 8 for all the cases discussed in Figure 7. Overall, relatively low levels of the velocity fluctuations are measured in the base flow upstream planes (Figures 8a and b), indicating a fairly stable initial rollup of the forebody vortices. While the vortical field at the next plane at $x'/D = 4$ (cf. Figure 7c) only hinted to the onset of asymmetry, the corresponding TKE field (Figure 8c) clearly indicates the onset of unsteadiness on the CCW side of the vortex pair. The increasing asymmetry in the TKE field is further seen at the next measurement plane (Figure 8d), showing a strong peak on the side of the formation of the secondary CCW vortex. As the CW vortex becomes detached

and displaced off the body in the last measurement plane (Figure 8e), its TKE signature weakens, compared to its still-attached CCW pair. Furthermore, continuing growth of the secondary CCW vortex indicates its formation coupling to the high unsteadiness. It is interesting to note that the secondary formation of the CW vortex actually lags its CCW pair, but appears to form with increased unsteadiness as well. The notable increase in the secondary vortex pair unsteadiness compared to their primary pair counterparts is attributed to their formation within the wake of the cylinder. As previously noted, anti-symmetry in analysis of the flow fields controlled by either the top right or top left 90° bleed segments (Figure 7), is even further supported by comparing the TKE fields over the first three measurement planes (Figures 8f–h vs. Figures 8k–m). Not surprisingly, the 'braid' of vorticity that feeds into the vortex on the side of the active bleed segment exhibits the elevated TKE. Past the initial vortex detachment from the surface, the remaining flow evolution becomes greatly affected by the surrounding wake, hence rendering the TKE distribution (just as the whole flow field) not exactly anti-symmetric, although the main features remain anti-symmetric throughout the measured planes. Thus, the first detached vortex remains marked by the elongated 'braid' of increased TKE, while the tilted surface-bound vortex remains fairly stable (Figures 8h and m). The overall unsteadiness seems to increase thereafter, after the second vortex detachment (Figures 8i and n), and in particular for the vortices measured in the farthest downstream plane (Figures 8j and o), which is again attributed to the increasing coupling to the growing wake of the cylindrical body, as the vortices progress downstream.

V. Bleed-Effected Flow Symmetry and Asymmetry

While the previous section focused on the most efficient flow control configurations for creating a net side force of either direction (and the accompanying yaw moments), the general assessment of the net effects of all eight bleed configurations (cf. Figure 6), points to another configuration that can potentially counter the pre-existing asymmetry in the flow and act to promote the flow symmetry and minimize the resulting net side force. Out of all the testing configurations, the one with the fully azimuthally open bleed over the forebody was the most successful with that respect. Hence, the remaining sections of this paper will focus on the detailed analysis of the representatives of the bleed control configurations that promote the flow symmetry (full azimuthal bleed) and asymmetry (top-right 90° bleed segment), in addition to the base flow, which is used as a reference case.

Since the resulting flow fields pertinent to the base and the top-right bleed segment were already discussed with respect to Figure 7, to contrast the characteristic three configurations here, only the flow fields in the most upstream and downstream planes are shown in Figure 9 for the base flow and the bleed control by the full and 90° segmented azimuthal bleed. Analogous to the flow fields previously shown in Figure 7, color raster plots of the mean streamwise vorticity overlaid with velocity vectors are shown at $x'/D = 1.6$ and 8.4. Clearly differently-evolving flow fields are seen immediately, in the most upstream plane, among all the three considered configurations. While the promoted asymmetry by the sectional bleed control (Figure 9c) relative to the base flow (Figure 9a) was noted earlier (cf. Figure 7), it is seen here that the full azimuthal bleed (Figure 9b) induces a rather dramatic change in the vortex evolution over the forebody, when compared to either of the other two cases. The full azimuthal bleed prematurely and symmetrically displaces both forebody vortices away from the surface, having the bleed contribution clearly marked by the elongated braids of vorticity connected to the primary vortices. Another important distinction is that the vorticity 'feed' off the surface becomes disrupted, and the primary vortices become weaker, having reduced circulation. The altered topology of the primary vortex pair formation

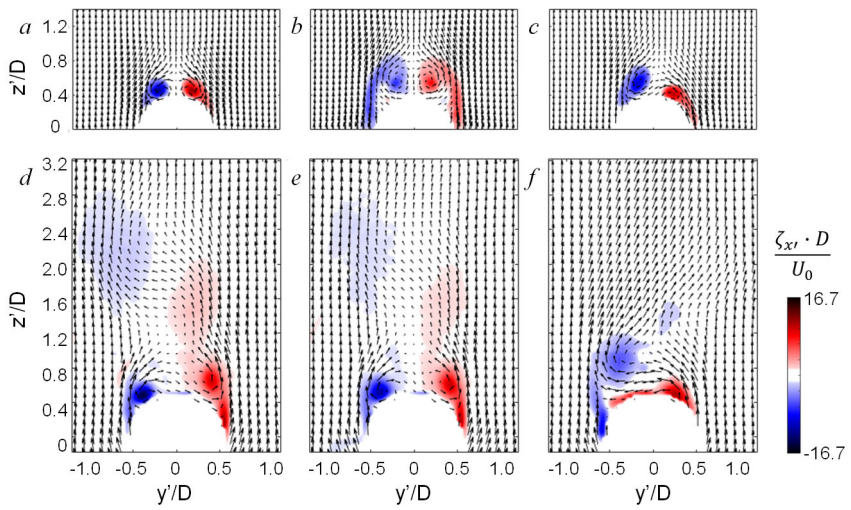

Figure 9. *Color raster plots of time-averaged streamwise vorticity concentrations overlaid with velocity vectors at x/D = 1.6 (a–c) and 8.4 (d–f) for the base flow (a, d) and with circumferential forebody bleed and segmented, right side forebody bleed (c, f).*

over the forebody is certainly carried through their ultimate detachment, although not shown in Figure 9 for brevity. It is interesting that at the most downstream measurement plane ($x'/D = 8.4$), despite the significant upstream differences, the base flow (Figure 9d) vortical composition and that in the presence of full azimuthal bleed become reasonably similar, although the circumferential bleed improves the overall wake symmetry, as seen in comparison of the wake flow fields above the body. The similar vortical composition of these secondary vortex pairs is attributed to the fact that the forebody bleed directly affects only the formation of the primary vortex pair and once this pair is detached, the remnants of the forebody flow control can affect the formation of the secondary vortex pair (seen in Figures 9d and e) only through their interaction with the altered wake, which is clearly only a secondary effect compared to the secondary vortex pair rollup around the downstream cylindrical body. Interestingly, when the bleed is intentionally asymmetric (i.e., restricted only to the right segment of the forebody, Figures 9c and f), not only that the CCW vortex on the bleed side becomes displaced away from the surface even over the forebody, as discussed in connection with Figure 7, but the profound change that this asymmetry induced in the upstream wake propagates all the way to the downstream end of the body (compare Figure 9f to Figures 9d and e). Not only that the formation of the secondary vortex pair does not restore to the process seen in the base flow, but both the vortical composition and the whole wake remains biased, which certainly contributes to the net side force attained in this control case, which is a cumulative effect of the whole flow field along the body.

Initial comparison between the three characteristic flow fields in Figure 9 is followed by the more detailed comparisons of the mean velocity distributions along the central vertical plane above the body. Such velocity profiles are extracted for all five measurement planes and for both the mean horizontal $U_{y'}$ and vertical $U_{z'}$ velocity components, and shown in Figure 10. Distributions of the horizonal velocity components are a good proxy for the flow symmetry assessment. Thus, it is seen in the base flow (Figure 10a) that the flow remains nearly perfectly symmetric in the first three measurement planes, as the horizontal velocity component remains virtually zero across the full vertical distribution. While both other velocity distributions return to zero at the upper end of the measurement domain, the symmetry disruption is clear towards the surface, where both distributions change signs, indicating a presence of the rotational motion in the mean. In accord with the prior analysis, these profiles indicate that the base flow develops asymmetry only at or after the initial primary vortex detachment. The overall improvement in the flow symmetry is suggested by the corresponding profiles for the full azimuthal bleed control (Figure 10b), although

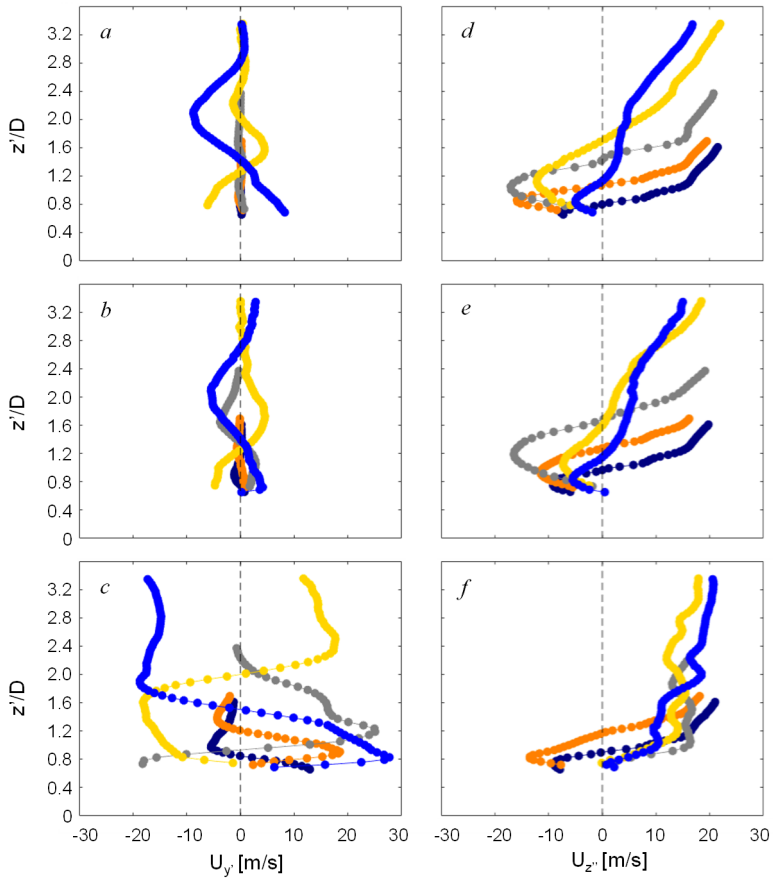

Figure 10. *Distributions of the in-plane side ($U_{y'}$, a–c) and vertical ($U_{z'}$, d–f) mean velocities along the plane of symmetry above the body for the base flow (a,d) and the flow controlled over the full azimuth (b,e) and by the 90° bleed segment over the top right (c,f), at x'/D = 1.6 (●), 2.2 (●), 4 (●), 6 (●), and 8.4 (●).*

there is some disruption of the initial symmetry already at the third measurement plane. Still, both of the most downstream planes appear to have the horizontal velocity excursions suppressed relative to the base flow. Finally, it is not surprising that analogous horizontal velocity profiles for the 90° top-right segment bleed (Figure 10c) are dramatically different than either of the other two cases. As the flow vortical composition becomes immediately biased, this is also reflected in the velocity distributions that are initially predominantly biased such that the flow is towards the displaced vortex, having a positive horizontal velocity component. The switch in the vortex detachment from the third to the forth, and then again to the fifth plane (Figure 7) is reflected in the switch of the horizontal velocity bias in Figure 10c, where the velocity profiles at $x'/D = 4$ and 8.4 are biased to the positive, while the profile at $x'/D = 6$ is biased to the negative horizontal velocity. Just as the central horizontal velocity component is shown to be a good indicator of the flow symmetry, and consequently a good predictor for the generation of the aerodynamic side force, the accompanying vertical velocity distribution suggests how the applied flow control may affect the bulk wake evolution, towards or away from the body. The two clear trends are seen in the vertical velocity profiles of the base flow (Figure 10d). First, although the near surface negative velocity points to the prevailing flow component towards the surface, it initially strengthens through the first three planes, and then relaxes. This is attributed to the initial vortex pair strengthening (in circulation) as they continuously 'feed' off the surface vorticity until they begin to displace away from the surface and their contribution to the near surface vertical velocity component begins to weaken. Secondly, as expected, a clear opening of the wake away from the surface is seen in the progressive stretching of the velocity profile with distance, while the velocity sign points to the direction away from the body. As seen in the corresponding profiles for the full azimuthal bleed case (Figure 10e), only a minor modification of the vertical velocity profile distributions is attained relative to the base flow case, which suggests that only a secondary modification of the bulk wake is attained by the full azimuthal control. Finally, just as in the case of the comparison of the horizontal velocity component, the vertical velocity distributions for the 90° azimuthal segment bleed (Figure

10f) is substantially different than in the other two cases. The local extent of the flow towards the surface becomes significantly suppressed in this case over the first two planes, followed by its complete suppression. Furthermore, the velocity sign switch is followed by a swift increase in the vertical velocity component away from the body.

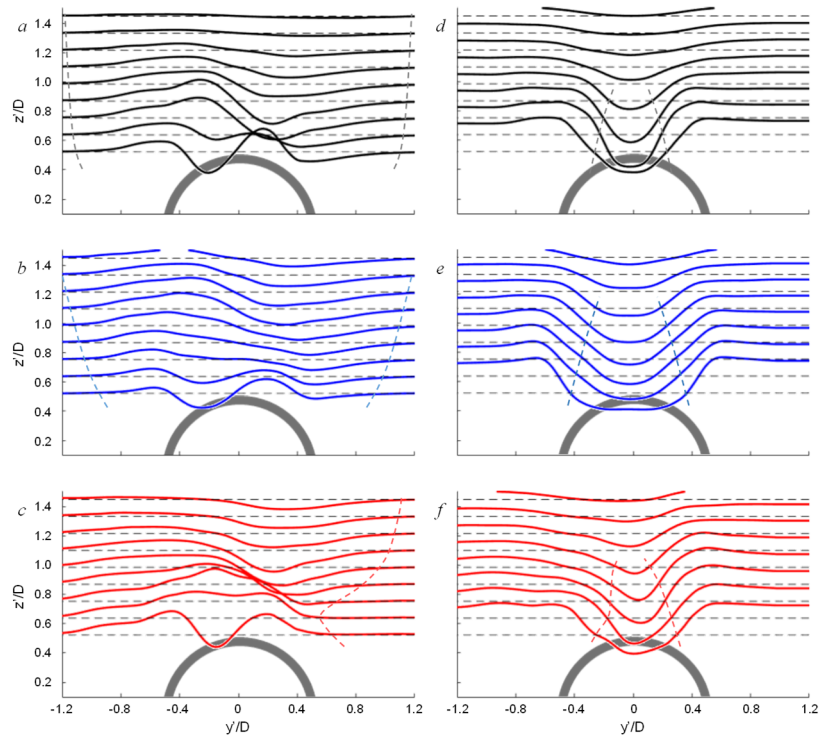

Figure 11. *Waterfall distributions of vertically-equidistant mean horizontal (a–c) and vertical (d–f) velocity components $U_{y'}$ and $U_{z'}$ for the base flow (a,d) and the flow controlled over the full azimuth (b,e) and by the 90° bleed segment over the top right (c,f) at $x'/D = 2.2$.*

Spanwise extent of the wake above the body is analyzed in Figure 11, where both the mean horizontal $U_{y'}$ and vertical $U_{z'}$ velocity profiles are shown as waterfall plots away from the body for the same three characteristic bleed configurations discussed in Figures 9 and 10. All the data are shown at $x'/D = 2.2$, which is the most downstream plane at which the full extent of the wake is captured within the measured field of view. Horizontal velocity component in the base flow (Figure 11a) indicates a fairly antisymmetric perturbation of this velocity due to the presence of forebody vortices, with the velocity slowly relaxing back to zero only at the outskirts of the measurement domain, as marked by the dashed lines. The corresponding vertical velocity distribution (Figure 11d) exhibits a typical wake structure that, instead to zero, relaxes back to the in-plane vertical velocity projection of the free stream, away from the center. A narrow domain of the reversed flow, towards the body, is marked by the dashed lines. As the full azimuthal bleed is activated, the spatial evolution of the mean horizontal velocity (Figure 11b) remains antisymmetric, but having attenuated excursions relative to the base flow. This attenuation also results in earlier relaxation of this velocity back to zero in the spanwise extent. Although the vertical component of the velocity excursions becomes also attenuated (Figure 11e), the bleed control also spreads the reversed flow region away from the body in either direction. As it can be expected, the asymmetric application of the segmented bleed (90° segment at the top right), biases the flow fields, which is particularly seen in the horizontal velocity component (Figure 11c). It is interesting that the disturbance to the horizontal velocity component is effected on the side opposite to the bleed actuation. While the horizontal velocity relaxes faster on the bleed side (marked by the dashed line), it practically does not fully relax up to the edge of the measurement domain on the opposite side. As already discussed in connection to Figure 7, this is attributed to the promoted roll-up and tilting of the vortex on the side opposite to the bleed actuation. Finally, in comparison of the vertical velocity component distribution (Figure 11f) relative to the base flow (Figure 11d), it seems that the reversed region of the wake does not significantly change, except of the whole wake

vectoring towards the unactuated side, only not as pronounced as it was the case of the horizontal velocity component.

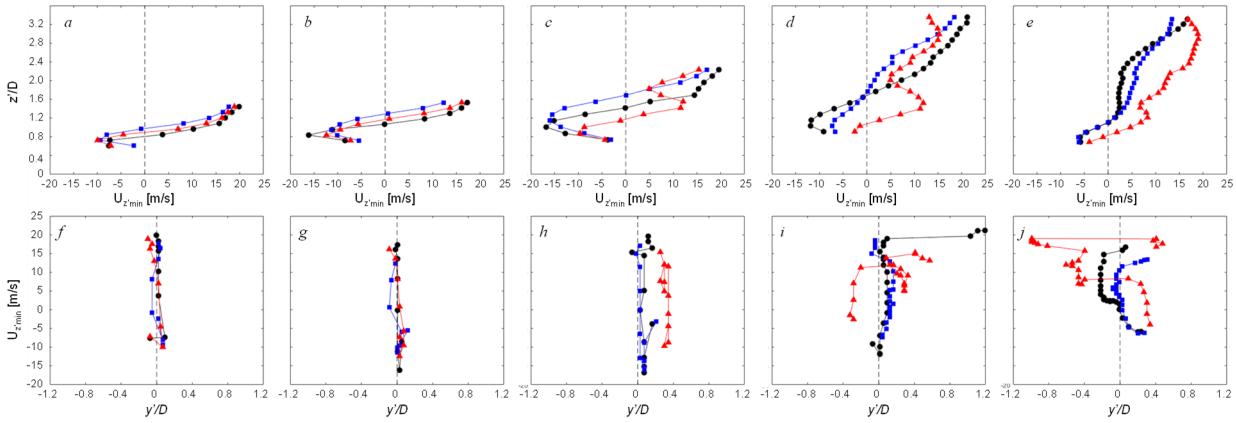

Figure 12. *Vertical (a-e) and horizontal (f-k) distributions of minimum streamwise velocity component $U_{z'min}$ at x'/D = 1.4 (a,f), 2.2 (b,g), 4 (c,h), 6 (d,i), and 8.4 (e,j) for the base flow (●), fully azimuthally opened (■), and 90° top-right (▲) azimuthal bleed configurations.*

Another characterization of the wake evolution through the five measurement planes is based on evolutions of the wake minimum streamwise velocity $U_{z'}$ distributions across the wake in the vertical (Figure 12a–e) and horizontal (Figure 12f–j) directions, for the three characteristic cases discussed in Figure 9. At the first measurement plane immediately downstream from the forebody (Figure 12a and f), no significant difference is measured among the three considered cases. Besides a slight increase in the recirculating extent of the near wake (Figure 12a), a typical downstream evolution of the wake is reflected in the increasing minimum velocity. In addition, the minimum velocity remains closely aligned with the axis of symmetry for all the three cases (Figure 12f), indicating that even in the case of induced vortical asymmetry (cf. Figure 9c), no significant side-tilt of the wake is effected. Even in the second measurement plane (Figure 12b and g), only a moderate expansion of the distributions observed in the first plane are noted, with no fundamental changes. By the third plane (Figure 12c and h), the aerodynamic bleed begins to substantially alter the natural wake evolution. In the vertical evolution of the minimum velocity (Figure 12c), the full azimuthal bleed expands the reversed flow extent relative to the base flow, while the top-right bleed application reduces it. While the other two configurations still nearly preserve the minimum velocity evolution along the axis of symmetry (Figure 12h), the asymmetric bleed control clearly offsets the minimum velocity/wake to the side of the bleed activation as the CCW vortex on that side is already shed off the surface. By the next-to-last measurement plane (Figure 12d and i), vortical asymmetry is developed in all the three configurations, which is reflected in all of the vertical distributions (Figure 12i). The sharp sideways deflections of the minimum velocity are related to the effect of the wake by the detached vortices, which is clearly the most pronounced in the most vertically-driven wake of the top-right bleed configuration. The corresponding vertical wake evolution indicates a nearly eliminated reversed flow for the top-right bleed. Finally, by the last measurement plane (Figure 12e and j), the full azimuthal bleed case does indicate the least departure from the minimum velocity alignment with the axis of symmetry (Figure 12j), while the top-right bleed case induces the widest shifts from one side to the other due to the strong shed vortices, while the vertical wake evolution of the minimum velocity indicates much stronger wake growth for the top-right case compared to the other two.

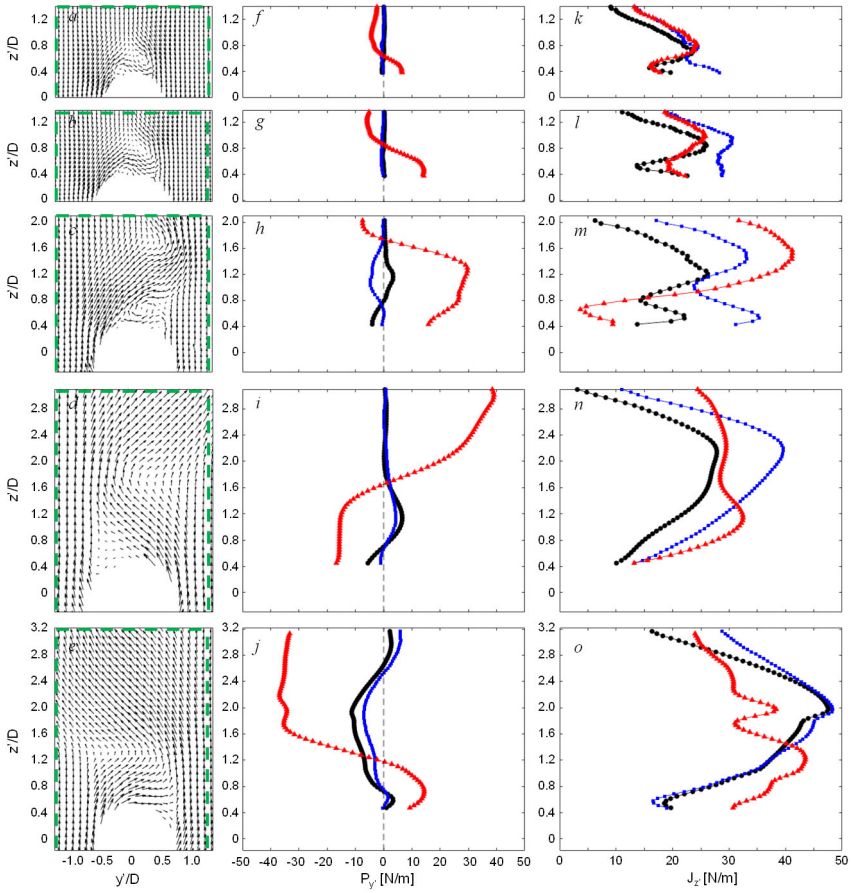

Figure 13. *Integral horizontal momentum flux (f-j) and vertical momentum deficit(k-o) with z' top dashed boundary variation (a-e) at x'/D = 1.4 (f,k), 2.2 (g,l), 4 (h,m), 6 (j,n), and 8.4 (k,o) for the base flow (●), fully azimuthally opened (■), and 90° top-right (▲) azimuthal bleed configurations.*

In addition to the analysis based on the velocity distributions, an integral analysis of the wake flow fields is also undertaken, primarily with an emphasis on the effects of the flow field structure in the wake on the net side force. To this end, the net horizontal momentum flux and vertical momentum deficit are assessed across a control volume depicted by overlaid dashed lines in each of the flow fields in Figures 13a–e. The evolution of the fluxes is assessed by varying the position of the top edge of the control volume (i.e., vertical expansion of the control volume) that captures the effects of the three-dimensional vortical flow structures within the wake on the fluxes. In this analysis, bottom edge of the control volume is taken to be sufficiently far below the model (outside of the field of view) with uniform free stream velocity across it. As shown in Figure 13f, in the first measurement plane only the top-right bleed leads to horizontal flux imbalance indicating the net flow contribution to the side force even as far upstream as at the tail end of the forebody. Interestingly, the momentum flux switches sign away from the body, a signature of the coherent vortical field switch, resulting in asymptotically small net effect for the sufficiently large control volume extent ($z'/D \approx 3.2$). The evolution of the net effect for the top-right bleed at the next plane (Figure 12g) is only amplified relative to the first plane, having the final net contribution of the same sign. It is interesting to note that by the third plane (Figure 13h), both the base flow and full azimuthal bleed begin to develop nonzero contributions to the horizontal flux; however, the net effect still asymptotes to zero far away from the body. Although a significant opposing horizontal flux is measured closer to the body, the net flux effect of the top-right bleed when the control volume extends away from the body is of the same sense as in the first two planes. While the other two configurations still do not indicate a net horizontal flux at the fourth plane (Figure 13i), there is a complete switch in the top-right bleed contribution, which reaches the opposing sign contribution at about fourfold magnitude than in the preceding planes. This strong change in the horizontal flux is clearly attributed to the antisymmetric vortical composition of this flow field relative to the three upstream fields (cf. Figure 7). Not surprisingly, another flip in the vortical composition of the flow field in the last measurement plane (Figure 7) results in the

corresponding flip in the net horizontal flux distribution. Interestingly, only at this last measurement plane, a small net contribution to the horizontal flux is seen for the base flow and for the full azimuthal bleed. Although assessed only over the five flow field snapshots, this analysis indicates that the net horizontal flux that ultimately leads to a net side force is strongly associated with the vortical wake composition, where different segment of the wake can locally impose side forces of opposing signs. Theoretically, if the forebody vortices would be shed in an antisymmetric time-periodic manner (akin to the Karman Vortex Street) along the body, it would be possible to attain a nearly zero net side force on the whole body, while body sections would be exposed to significant switching side forces along its axis. The other suggestion of the present analysis is that the net side force in the weakly asymmetric vortex 'shedding' off the axisymmetric body is predominantly associated with its tail-end wake.

Another integral measure of the controlled and uncontrolled wake evolution is based on the momentum deficit of the normal component of the freestream flow, which in a 2-D flow over a spanwise cylinder would be associated with drag. Clearly, in the present case the flow is three-dimensional, and the wake grows along the body. As already stated above, the oncoming free stream flow projection from below (outside of the measurement domain) is taken to be uniform, while the momentum flux above the body is based on the momentum variation across the body-normal coordinate z'. Thus, momentum deficit distributions with increasing distance away from the body are shown in Figures 13k–o analogous to the flux distributions shown in Figure 13f–j. Regardless of the measured plane or the control configuration, it is clear that no asymptotic deficit is reached even farthest away from the body ($z'/D \approx 3.2$) and that, along with the wake growth along the body, each successive downstream wake section exhibits increasing momentum deficit. In addition, each of the distributions of the momentum deficit is strongly affected by the vortex-induced artifacts of the flow; namely, the local peaks of the deficit are associated with the opposing effects that the vortex pair suppresses or even reverses body-normal flow. For instance, the local momentum deficit peak at $z'/D \approx 0.6$ in the base flow (Figure 13k) is associated with the reversed flow induced by the forebody vortex pair seen in Figure 7a. Further away from the body, these local peaks are typically associated with a strong wake sidewise vectoring (that also contributes to the net horizontal momentum change), such as in the base flow at $z'/D \approx 2.1$ in Figure 13o (cf. Figure 7e). Overall, not surprisingly, the most momentum deficit through the measured flow fields is associated with the full azimuthal bleed, as suggested by the observed wake evolution in Figures 9 and 11. It is interesting to note, though, that since the far wake evolutions, past the initial vortex pair detachment, are fairly similar between the base and the full-azimuthal bleed flows (compare the flow fields in Figures 9d and e), this previous observation is strongly supported by the nearly overlapping distributions in Figure 13o.

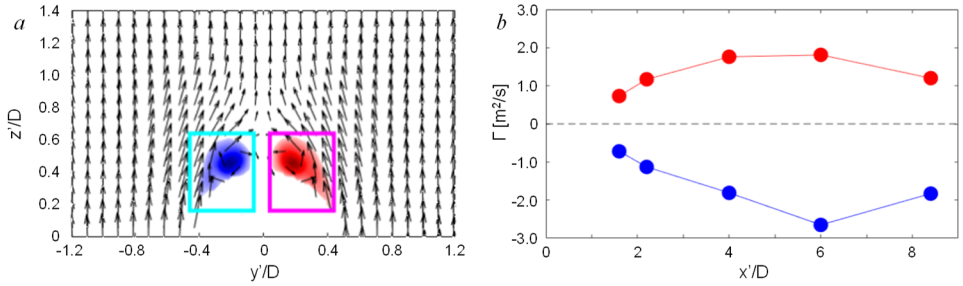

Figure 14. *An illustration of the vortex bounds for the integral calculation of the CW and CCW vortex circulations (a) and the corresponding circulation evolution of each vortex for the base flow (b).*

An integral measure of the flow control effect on the forebody vortex pair evolution is further sought through the estimates of evolution of each vortex circulation through the five PIV measurement planes. Based on each ensemble-averaged PIV flow field, two primary vortices are first isolated, as illustrated in Figure 14a. Once the vortical bounds are set, their total circulation was calculated as an integral measure of the product of the local vorticity component $\zeta_{x'}$ and the unit area $dA' = dy'dz'$. The resulting circulation evolution of the forebody vortices in the base flow in shown in Figure 14b. As expected, based on the analysis of Figure 7, circulations of both the CCW and CW vortices are of the same magnitude up to the third measurement plane. The vortical imbalance seen in Figure 7d is clearly reflected in the corresponding circulations at $x'/D = 6$ in Figure 14b. After the primary vortices become detached (Figure 7e), its circulation weakens, as seen in Figure 14b, while the CW circulation still remains higher than its counterpart CCW circulation. However, from the standpoint of the force exerted on the body, detached vortex influence diminishes with distance, and circulation of the secondary vortices becomes more important than the primary ones, once both of the primary vortices are detached.

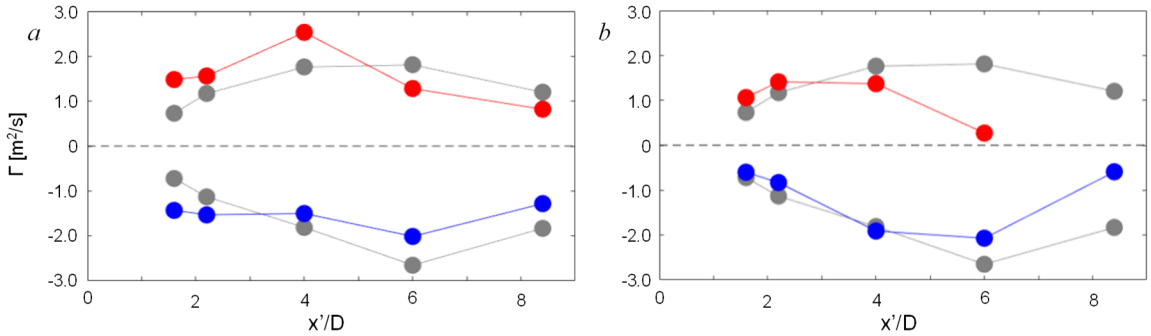

Figure 15. *Evolution of the circulation for the forebody CW (■) and CCW (●) vortices for the bleed control over the full forebody circumference (a) and over the 90° top-right segment (b). Corresponding circulations of the base vortices as shown in grey for reference.*

Changes in circulation of the primary vortices due to the full and segmented azimuthal bleed configurations considered in Figures 9–13, relative to that of the base flow vortices, are shown in Figure 15. In either case, the base flow circulations are shown in grey as a reference. The overall effect of the full azimuthal bleed (Figure 15a) is seen in the closer balancing of the circulation magnitudes of both vortices, which is another indication of the enhanced symmetry of the flow. Although the circulation magnitudes at the first two measurement planes indicate that the total CCW and CW circulation magnitudes are increased relative to the base flow, it should be noted that these total circulations include a rather strong vorticity braids that feed off the bleed ports and are connected to the vortices (cf. Figure 5b) and therefore become included into the vortical structure detected on either side. It is clear that without the braids, the vortices themselves do not necessarily carry more circulation than their counterparts in the base flow. This is further illuminated in the downstream evolution when the direct feed from the bleed becomes disconnected, and the results at the two most downstream planes indicate that the circulation of the controlled vortices is lower than that of the base flow. Circulation evolution is markedly different when the bleed is applied only over the 90° top-right azimuthal segment (Figure 15b). Initially, a small increase in circulation is measured over the CCW vortex on the side of the active bleed, again enhanced by the promoted braid of vorticity from the bleed surface, while a minute reduction in the CW circulation on the opposite side might be associated with some enhanced spreading and tilting of the CW vortex pair on the opposite side. By the third measurement plane at $x'/D = 4$ (cf. Figure 7h), the CCW vortex is

already detached and its circulation remains nearly constant to that at $x'/D = 2.2$, while the CCW vortex remains attached and builds up circulation. By $x'/D = 6$, the CCW vortex is mostly gone from the field of view and its circulation is consequently low, while the CW vortex becomes detached and subsequently its circulation does not get notably changed from the previous one at $x'/D = 4$. By the last measurement plane, the CCW vortex is completely out of the field of view, while only a small remnant of the CW vortex within the field of view amounts to the low circulation magnitude. Overall, a strong imbalance in the primary vortex pair circulation around the body clearly induces a net side force, as the forebody vortices have a major contribution to the net side force.

As already noted, besides the primary forebody vortices, a secondary vortex pair forms over the body, once the primary vortex pair detaches off the surface. From the vortex contributions to the net changes in side forces, it is desired to follow and consider the vortices that are bound or close to the surface, i.e., the forebody vortices up to their lift off, and the secondary vortex pair downstream from that point. To place emphasis on the major vortical contributions to the aerodynamic forces (and moments), Figure 16 isolates only the vortical structures around the body at all five measurement planes, for the base (Figure 16a-e) and the flow controlled by the full azimuthal (Figures 16f-k) and 90° top-right segmented (Figures 16l-p) bleed. In addition, surface-tangential mean velocity profiles with respect to the wall-normal direction that pass through either vortex (marked in dashed lines) are overlaid on the plots. As such dashed lines also represent the azimuthal orientation of the vortices, it is seen that the azimuthal orientation of the forebody vortex pair remains fairly stable (Figures 16a-c), with the weakening of the velocity perturbation near the surface with the vortex stretching and with their approach to detachment. Also, perturbations of both vortices remain antisymmetric and clearly indicate the equal but opposing effect. By $x'/D = 6$ (Figure 16d), both primary vortices appear fairly diffused

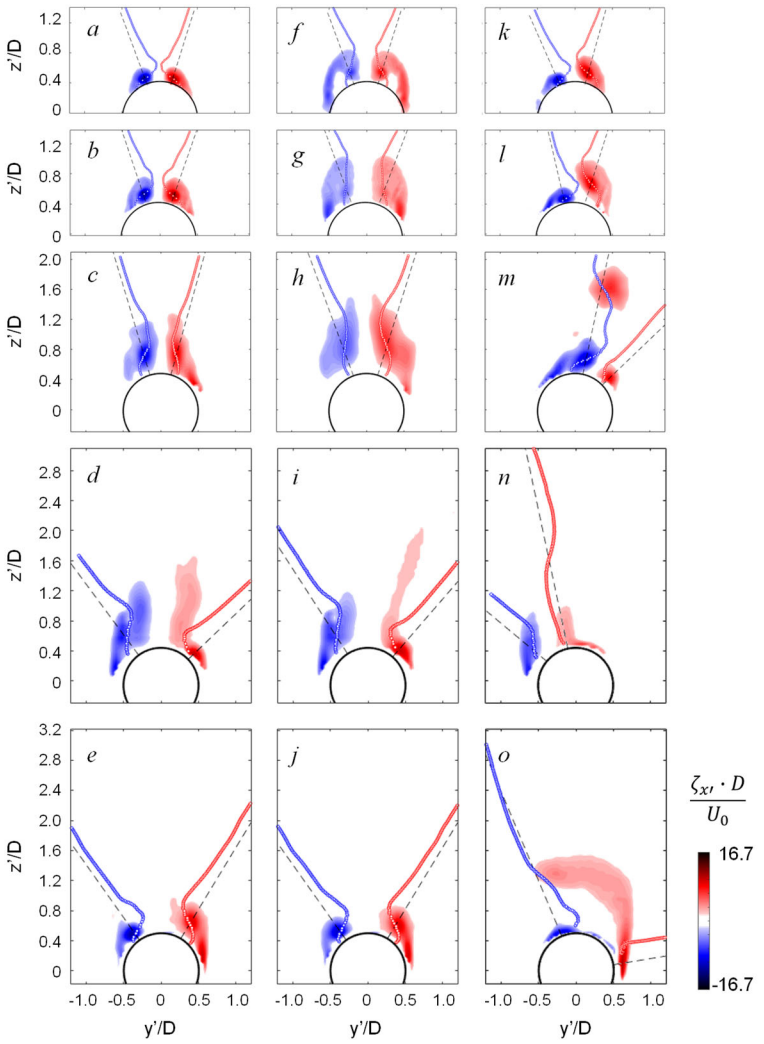

Figure 16. *Raster plots of the mean streamwise vorticity $\zeta_{x'}$ and in-plane velocity profiles intersecting the vortex cores at $x'/D = 1.4$ (a,f,k), 2.2 (b,g,l), 4 (c,h,m), 6 (d,i,n), and 8.4 (e,j,o) for the base flow (a–e) and for the full azimuthal (f–j) and the top-quarter right (k–o) bleed configurations.*

in the average, attributed to their increased unsteadiness (cf. Figure 8d). The peak velocity perturbations are displaced away from the surface, while the near-surface perturbation weakens. Finally, the vortical velocity perturbation near the surface is notably stronger on the CCW vortex side at the last measurement plane, with both vortices remaining spaced much more apart azimuthally than for the forebody vortices. Although structurally fairly similar to the base flow, there are secondary modifications of the forebody vortical perturbation of the near-surface flow when the full azimuthal bleed is applied (Figures 16f-h). Along with the extended outboard reach of the perturbations, their excursions near the surface lessen, in addition to the slightly increased azimuthal spacing of the vortices. There are even more similarities of the vortical perturbations associated with the downstream fields (Figures 16i and j), as the direct flow control effects terminated far upstream from these axial locations, and the convecting changes of the wake from upstream are rather mild. Lastly, as expected, velocity perturbations along the surface become notably asymmetric for the forebody vortex evolution under the segmented 90 top-right bleed (Figures 16k-m). Initially (Figure 16j), strong growth of the vortex on the bleed side induces the accordingly strong increase in the velocity along the surface on its side, while the uncontrolled-side vortex contribution does not appear much different from that of the base flow. However, further disbalance in the vortex growth affects not only the bleed-side perturbations, but also that on the opposite side, as the CW vortex begins to roll and tilt at $x'/D = 2.2$ (Figure 16l), such that not only the CCW vortex contribution is increased relative to the base flow, but the CW vortex' opposing contribution weakens. By the next measurement plane (Figure 16m), not only that there is an imbalance in velocities near the surface but the vortex pair becomes tilted to the bleed side, further increasing the uneven net contribution to the aerodynamic side force. This observed tilt completely changes after detachment of the CW primary vortex (Figure 16n), when the perturbation balance switches side. Nonetheless, velocity perturbations near the surface seem to be rather small. Lastly, it appears that the phase delay between the secondary vortex formations on the cylinder sides increases by the last measurement plane (Figure 16o) and the vortex pair azimuthal switch to the opposite side appears incomplete.

VI. Optimized Forebody Bleed Actuation

After the initial study of the bleed flow control effectiveness presented in Sections IV and V, the bleed configuration about the forebody was redesigned, keeping the same porosity. To check for the resulting flow control effectiveness, a sweep in the body pitch angles was performed first, ranging from $35° < \alpha < 55°$. Following the discussion in Section IV, the two configurations inducing the largest excursions in the side force are first tested at each pitch angle – a 90° azimuthal segment positioned at the top right and left, i.e., directly affecting only the CCW and CW vortex, respectively, as previously seen in Figure 7. The resulting aerodynamic forces relative to the fixed coordinate system (x, y, z) are shown in Figure 17a. In principle, both the effect on drag and lift should not depend on the side at which the bleed control is applied. While the lift data are practically overlapped for the right- and

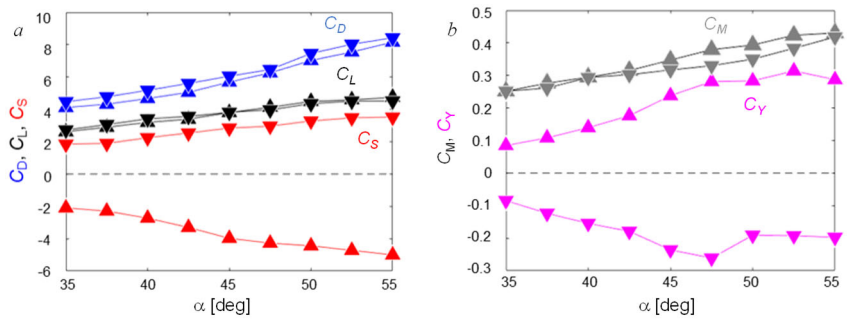

Figure 17. *The net aerodynamic force (a) and moment (b) coefficients for the 90° open bleed segments centered at the top right (up triangle) and left (down triangle).*

left-side flow control, there is a small by consistent offset in the drag results. As for the most interesting aerodynamic effect – the side force, progressively increasing side force is achieved with the pitch angle, with the sign defined by the side of the bleed control application, in accord with the studies already shown in Section IV. The difference relative to the results shown in Figure 6 is that the side force coefficients reach or even exceed $C_S = 4$, which nearly match the lift coefficient at higher angles of attack. As discussed in analysis of Figure 6 earlier, some discrepancy in the attained magnitudes for the opposite-side actuation can be attributed to the non-zero base flow side force, i.e., to the fact that the base flow is biased towards the one-side asymmetry (that results in the net positive C_S in this case) in the absence of the flow control. Similar to the analysis of Figure 6, as almost exclusive change in the aerodynamic forces in Figure 17a is in the side force direction, the associated moments change is in the yaw (in the fixed coordinate system), as seen in Figure 17b. Some discrepancy in the pitch moments that result from the bleed control by the top right and top left orientations are the direct consequence of the offset in drag seen in Figure 17a.

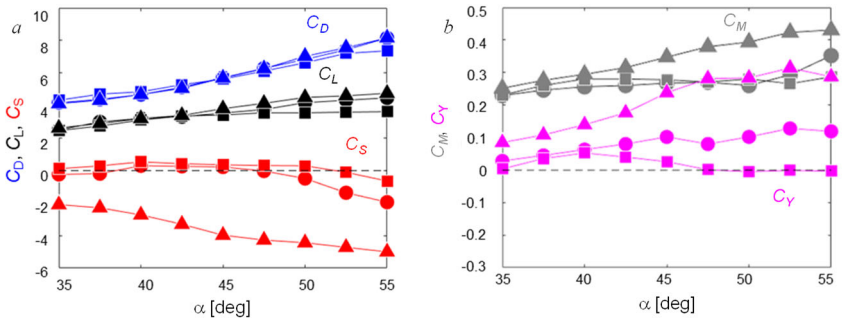

Figure 18. *Variation with α of the aerodynamic force (a) and moment (b) coefficients for the base flow (circle) and with the full azimuthal (square) and the 90° top-right segmented forebody bleed (triangle).*

Similar to the earlier analysis of the effects of the two characteristic bleed configurations (cf. Section V), the representatives of the bleed control configurations that promote the flow symmetry (full azimuthal bleed) and asymmetry (top-right 90° bleed segment), are also assessed with the revised bleed configuration, with addition of the base flow, as a reference case. Hence, the corresponding evolution of the lift, drag and side force coefficients with angle of attack is shown in Figure 18a for the baseline flow and the bleed configurations of Figure 9, while the corresponding changes in pitch and yaw moments are shown in Figure 18b. As expected, both C_D and C_L increase monotonically over most of the range of α, where the rate of increase in C_L begins to diminish past $\alpha > 45°$as the forebody vortices begin to lift off the cylinder surface and the flow from the windward separates on its leeward surface. The side force coefficient C_S in the base flow is nearly zero as long as there is no major asymmetry in the evolution of the forebody vortices, but when the symmetry breaks for $\alpha > 45°$, there is an increase in the magnitude of the net side force. Since for this forebody the CCW vortex is the first to become detached from the surface, the net side force is negative. As seen earlier in Figure 7, the symmetry-enforcing full circumferential azimuthal bleed is therefore expected to alleviate some of the net side force of the base flow, which is particularly evident at these high inclination angles. Along with the reduction in the side force, this bleed actuation also slightly reduces both the lift and drag at these high α. Finally, as expected, the strong flow asymmetry induced by the segmented bleed (cf. Figure 7) is accompanied by a strong net side force whose magnitude increases with α, while the lift and drag remain nearly unchanged relative to the base flow. The benefits of the full azimuthal bleed are presumably even better expressed in the net yaw moment (Figure 18b), where the increasing yaw moment of the base flow for higher elevation angles becomes diminished back to zero under the full azimuthal bleed control.

VI. Conclusions

The present experimental investigations build on the earlier investigations of Lee et al. (2021a, 2021b), who demonstrated the receptivity of the wake of slender axisymmetric bodies at high incidence to direct control of the near wake by affecting its interaction with the forebody vortices and thereby the resulting aerodynamic side force and the yawing moment. In contrast to the *indirect* control of the effects of the forebody vortices on the aerodynamic loads, the present investigations focus on *direct* control of their formation and evolution by segmented distributed aerodynamic bleed over the forebody surface of the wind tunnel model (diameter $D = 50$ mm, length $L = 9D$, $35° < \alpha < 55°$, $Re_D = 9.9 \cdot 10^4$). The present investigation is motivated by the earlier findings of Bauer and Hemsch (1994) who demonstrated that azimuthally-uniform bleed over the forebody can lead to suppression of the instabilities that lead to the random evolution of asymmetric side forces. The present investigations focuse on exploiting segmented porosity over the forebody of a cylindrical platform not only for suppression of asymmetric side forces that arise from flow's receptivity to minor imperfections of the body surface but, more importantly for prescribing desired side forces and yawing moment for bi-directional aerodynamic control.

It is shown that segmented azimuthal bleed actuation over the forebody can lead to significant changes in the evolution and symmetry of the forebody vortex pair that are accompanied by controllable side forces of prescribed sense. Bleed control can be used to overrides naturally evolving forebody flow asymmetries and can either amplify the resulting induced loads or suppress them by manipulation of the forebody vortices. This finding is of particular significance considering the receptivity of the base forebody flow to small surface and flow nonuniformities. Depending on the angle of incidence, bleed-induced side force coefficient increments as high as $\Delta C_S = \pm 3.5$ can be attained where, by comparison, the corresponding `vertical (lift) coefficient is $C_L \approx 4.5$.

The wake flow features associated with the base and controlled realizations of the aerodynamic loads are elucidated using successive PIV measurements that revealed the evolution of streamwise vortical structures along the body. It is shown that weakly asymmetric forebody vortices in the base flow, primarily induce the unbalanced side loads over the downstream end of the body, following the first forebody vortex detachment. Full azimuthal bleed control alters the vortical evolution over the forebody by the equal vortex displacement off the body and thereby severing the off-surface vorticity influx, while maintaining the left-to-right flow symmetry. In contrast, segmented one-sided bleed directly affects the adjacent forebody vortex, inducing an aerodynamic imbalance while the opposite side vortex responds to the wake of the detached vortex by tilting in its direction. The detachment of the primary vortices is followed by successive rollup and interactions of secondary vortices along the cylinder's wake.

Acknowledgment

This work was supported by the Army Research Office, monitored by Dr. M. Munson.

References

Allen, J. H. and Perkins, E. W., "Characteristics of Flow over Inclined Bodies of Revolution," NACA RM-A50L07, 1951.

Bauer, S. X. S. and Hemsch, M.J., "Alleviation of Sideforce on Tangent-Ogive Forebodies Using Passive Porosity," *Journal of Aircraft*, Vol 31, No 2, 1994, pp. 354-361.

Chapman, G.T., Keener, E.R., and Malcolm, G.N., "Asymmetric Aerodynamic Forces on Aircraft Forebodies at High Angles of Attack - Some Design Guides," AGARD Conference Proceedings AGARD-CP-199 (12), 1976.

DeSpirito, J., "CFD Aerodynamic Characterization of 155-mm Projectile at High Angles-of-Attack," *AIAA Paper* 2017-3397, 2017.

Ericsson, L. E. and Reding, J. P., "Asymmetric Vortex Shedding from Bodies of Revolution," *Progress in Astronautics and Aeronautics, Tactical Missile Aerodynamics*, Vol. 104, 1986, pp. 243-296.

Ericsson, L.E. and Reding, J.P., "Alleviation of Vortex-Induced Asymmetric Loads," *Journal of Spacecraft and Rockets,* Vol. 17, No. 6, 1980, pp. 546-553.

Fears, S. P., "Low-Speed Wind-Tunnel Investigation of a Porous Forebody and Nose Strakes for Yaw Control of a Multirole Fighter Aircraft," *NASA CR-4685*, 1995.

Keener, E. and Chapman, G., "Onset of Aerodynamic Side Forces at Zero Sideslip on Symmetric Forebodies at High Angles of Attack," *AIAA Paper 74-0770*, 1974.

Kumar, R., Viswanath, P. R., & Ramesh, O. N, "Nose Blowing for Side Force Control on Slender Cones at High Incidence," *Journal of Aircraft*, Vol. 45, No. 5, 2008, pp. 1156-1166.

Lambert, T.J., Vukasinovic, B., and Glezer, A., "A Six Degrees of Freedom Dynamic Wire-Driven Traverse," *Aerospace* Vol. 3: 11, 2016.

Lamont, P. J., "Pressures Around an Inclined Ogive Cylinder with Laminar, Transitional, or Turbulent Separation," *AIAA Journal*, Vol. 20, No. 11, 1982, pp. 1492-1499.

Lee, E., Huang, Y., Vukasinovic, B., and Glezer, A., "Controlled Aerodynamic Loads on a Slender Axisymmetric Body at High Incidence," *AIAA Paper* 2021-1943, 2021a.

Lee, E., Huang, Y., Vukasinovic, B., and Glezer, A., "Aerodynamic Flow Control of an Unstable Slender Cylindrical Body at High Incidence," *AIAA Paper* 2021-2610, 2021b.

Leu, T.-S., Chang, J.-R. and Lu, P.-J., "Experimental Investigation of Side Force Control on Cone-Cylinder Slender Bodies with Flexible Micro Balloon Actuators," *Exp. Ther. Fl. Sci.*, Vol. 29, No. 8, 2005, pp. 909-918.

Mahadevan, S., Rodriguez, J., and Kumar, K., "Effect of Controlled Imperfections on the Vortex Asymmetry of a Conical Body," *AIAA J.*, Vol. 56, 2018, pp. 3460-3477.

Taligoski, J., Uzun, A., and Kumar, R., "Effect of Roll Orientation on the Vortex Asymmetry on a Conical Forebody," *AIAA Paper* 2015-0547, 2015.

Thomson, K.D. and Morrison, D.F., "The Spacing, Position and Strength of Vortices in the Wake of Slender Cylindrical Bodies at Large Incidence," *J. Fluid Mech*, Vol. 50, 1971, pp. 751-783.

Xueying D., Xuerui C., Yankui W., and Peiqing L., "Influence of Nose Perturbation on Behaviors of Asymmetric Vortices over Slender Body," *AIAA Paper* 2002-4710, 2002.

Yanta, W. and Wardlaw, A., "Laser Doppler Velocimeter Measurements of Leeward Flowfields on Slender Bodies at Large Angle-of-Attack," *AIAA Paper* 77-0668, 1977.

Yanta, W. and Wardlaw, A., "Flowfield about and Forces on Slender Bodies at High Angles of Attack," *AIAA J.*, Vol. 19, No. 3, 1981, pp. 296-302.

Zilliac, G. G., Degani, D. and Tobak, M., "Asymmetric Vortices on a Slender Body of Revolution," *AIAA J.*, Vol. 29, No. 5, 1991, pp. 667-675.